Construction and Monitoring of a Quantitative Inversion Model for Conductivity Using Unmanned Aerial Vehicle Remote Sensing Based on ELM Algorithm

Yuanhai Li
School of Electrical Engineering, Ganzhou Polytechnic, Ganzhou 341000, China
E-mail: liyuanhai8805@163.com

Keyword: Extreme learning machine; Conductivity; Unmanned aerial vehicle; Remote sensing technology; Machine learning; Support vector machine

Received: June 13, 2024

Currently, unmanned aerial vehicle remote sensing technique has wide application in agricultural soil salinization monitoring. However, there are still issues such as high costs and complex data preprocessing. Based on this, the research is conducted on the unmanned aerial vehicle multispectral image. The ground synchronous acquisition of soil conductivity is regarded as the data source. The multispectral image spectral characteristics and texture characteristic information of the unmanned aerial vehicles is extracted through the gray symbiotic matrix method and Gabor two-dimensional filter. The soil conductivity of unmanned aerial vehicle remote sensing quantitative inversion model is established combined with the limit learning algorithm. The results showed that the mean, variance, homogeneity, contrast, dissimilarity, entropy, second-moment, and correlation had good association. The correlation coefficient was between 0.17 and 0.35. However, the correlation of the mean, variance, homogeneity, and entropy was significantly higher than the remaining indices. The salinity indices ARVI, SI-T, NDSI, S6, S1, S3, S5, S2, SI3, and SI2 showed positive correlations with soil conductivity. The correlation coefficient was between 0.19 and 0.67. The quantitative inversion model of soil conductivity based on limit learning machine algorithm was constructed by fusing spectral feature and texture feature information. Its modeling set coefficient of determination was 0.77, 0.82, and 0.86, respectively. Its prediction sets coefficient was 0.73, 0.77, and 0.80. The model had the highest prediction accuracy compared with the texture feature model and the spectral index model. Through information fusion, the prediction accuracy of the model was significantly improved. The results show that the unmanned aerial vehicle remote sensing monitoring model of soil salinity can be constructed by using the algorithm. This study has certain technical guidance value for unmanned aerial vehicle remote sensing monitoring of soil salinization

Povzetek:Članek raziskuje uporabo brezpilotnih letal za daljinsko zaznavanje in kvantitativni model za inverzijo prevodnosti tal s pomočjo algoritma Extreme Learning Machine (ELM). Model, ki združuje spektralne in teksturne značilnosti, je kvalitetno napovedoval prevodnost tal, kar ima pomembno vrednost za spremljanje slanosti tal v kmetijstvu.

1 Introduction

Under the influence of natural or human factors, the surface layer's salt content of soil continues to increase. The phenomenon of saline alkali disasters formed when the soil salinity ≥ 0.3% is called soil salinization. As a global ecological and environmental issue, soil salinization has received widespread attention from researchers and governments around the world [1, 2]. The main manifestation of soil salinization in China is the uneven distribution of water and salt. This is because during soil salinization, local areas experience changes in water movement due to the impact of precipitation, surface water, groundwater, and other factors on the surface or changes in groundwater levels. Finally, the phenomenon of salt moving towards the surface with water is caused [3, 4]. Due to the combined effects of natural and human factors, soil salinization is gradually deteriorating. Natural factors include temperature, precipitation, terrain, vegetation, etc. Human factors include fertilization, cultivation, irrigation, and other human activities. Salt accumulation in soil causes changes in soil physical, chemical, and biological aspects. Salt accumulation seriously affects the growth and development of crops, reduces soil nutrient availability, and ultimately reduces crop yield and quality [5-7]. It should implement precise saline soil treatment plans and soil salinization prevention and control measures to prevent the expansion of soil salinization scale. Accurately obtaining information on soil salinization is a fundamental prerequisite for formulating saline soil treatment plans and prevention and control measures. Indicators that can characterize soil salinization information are obtained by utilizing modern technological means. Improving the accuracy of soil salinization monitoring is crucial for soil salinization prevention and control [8].

The conventional soil salinity detection methods obtain data from point sources, which has the limitation of

spatial discontinuity. This is not conducive to obtaining detailed spatial distribution information of soil salinization, which consumes a lot of time and manpower. The development of satellite Remote Sensing (RS) technology offers a novel method for quickly obtaining soil salinity information. Satellite RS technology can estimate soil salinity on a large scale, quickly, and without damage. The satellite RS technology is widely applied in soil salinity monitoring, providing strong technical support for soil salinization research [9, 10]. However, with the developed precision agriculture, satellite RS spatial and temporal resolution can no longer meet the demand. Especially for single farmland, this technology cannot provide more accurate and cost-effective spatial information. Unmanned Aerial Vehicle (UAV) RS technique has wide application in large-scale terrain mapping, land use surveys, and environmental monitoring [11, 12]. The UAV RS technology can carry out shooting work in large areas. RS operations are simple. The UAV RS technology is less affected by terrain and weather factors, which can compensate for the shortcomings of satellite RS [13, 14].

In agricultural RS, multispectral UAV RS is commonly used. This RS system is composed of a multispectral camera carried by UAV that can be used to obtain the main health indicators of crops. Its images can extract vegetation indices, reflectance, and digital surface models, among others. Meivel et al. used normalized differential vegetation index and near-infrared band sensors for UAV RS analysis in multispectral views of agricultural land. The standard irrigation level was 60%. The correlation between plant growth $p \leq 0.01$ [15]. Webb et al. tested a relatively new method for identifying acidic soil regions using UAV, which linked UAV observations of normalized vegetation indices with field measured soil pH values to determine soil acidity regions [16]. Sahoo et al. proposed a UAV RS wheat nitrogen assessment method based on hyperspectral sensors and machine learning. The training, validation, and testing values for plant nitrogen assessment using this method were 0.97, 0.84, and 0.86, respectively [17]. Lednev et al. proposed a UAV fluorescence LiDAR for agricultural field diagnosis. On site testing demonstrated the feasibility and prospects of UAV autonomous LiDAR sensing, which could be used for early detection and on-site positioning of plants under pressure [18]. Table 1 summarizes the previous research on the quantitative inversion model of conductivity UAV RS.

Table 1: Summary of previous research

Scholar	Methodology	Key results	Limitations
Gojiya et al. [10]	This article provides an overview of soil salinity estimation methods based on RS and GIS, including salinity index, vegetation index, regression method, neural network, RS, and satellite data used for soil salinity mapping.	The RS technology is more cost-effective and efficient than traditional methods.	The choice of mapping method depends on the context and requires further research.
Cui et al. [12]	Neural network, random forest, and multiple linear regression algorithms are used to establish SSC estimation models.	A fast and low-cost time series method for monitoring soil salinization in sunflower fields has been proposed.	The accuracy of soil salinization detection in sunflower farmland needs to be improved.
Guo et al. [13]	8 different feature space monitoring indices based on Landsat TM/ETM+/OLI images are constructed.	A model for optimal monitoring indicators of soil salinization is proposed based on field observation data.	This study lacks practical application explanations.
Pal et al. [14]	A new model for license plate number detection in UAV images is constructed using Swin transformer.	The performance of the model is further improved under adverse conditions such as degradation, poor quality, and occlusion.	The accuracy of UAV image detection needs to be further improved.
Meivel et al. [15]	Normalized differential vegetation index and near-infrared band sensors are used for UAV RS analysis in multispectral views of agricultural land.	The standard irrigation level is 60%. The correlation between plant growth $p \leq 0.01$.	There are few testing indicators for research models.
Webb et al. [16]	A relatively new method for identifying acidic soil regions is constructed using UAV.	The UAV observations of normalized vegetation indices are linked with field measured soil pH values to determine soil acidity	Only studying soil acidity regions is relatively one-sided.

		regions.	
Sahoo et al. [17]	A UAV RS wheat nitrogen assessment method based on hyperspectral sensors and machine learning is constructed.	Training, validation, and testing values for plant nitrogen assessment using this method are 0.97, 0.84, and 0.86.	There is a significant gap in the training, validation, and testing values of plant nitrogen assessment. The accuracy of the model needs further improvement.
Lednev et al. [18]	A UAV fluorescence LiDAR for agricultural field diagnosis is constructed.	The method can be used for early detection and on-site positioning of plants under pressure.	The method is only useful in the early stages of crops, lacking full cycle application examples.

Machine learning algorithms are also a technique for estimating soil Electrical Conductivity (EC), with the characteristics of generating adaptive and robust relationships. In the soil salinity monitoring model of UAV spectral RS, Extreme Learning Machine (ELM) has achieved good results, with advantages such as high accuracy and fast speed [19]. As a result, the UAV RS technique has wide application in agricultural RS. This technology allows for flexible selection of time to obtain data, high monitoring accuracy, and convenient processing. However, there are still issues such as high cost and complex data preprocessing. A quantitative inversion model for EC UAV RS based on ELM is established in this study.

2 Methods and materials

Firstly, Gray-level Co-occurrence Matrix (GLCM) is utilized. Gabor two-dimensional filters are introduced to extract the preprocessed RS images' texture and spectral features in the study area. Then ELM is combined to construct an EC UAV RS quantitative inverse model based on ELM.

2.1 Data Collection and preprocessing

The research area is located in location A, with geographic center coordinates of 40°45′~41°60′N and 440°45′~41°60′N, belonging to a continental warm temperate arid climate. The research area has saline soil, with an average annual temperature of 10.8 ℃, an annual evaporation of 1992.0~2863.4mm, and an annual precipitation of 46.4~64.5mm. This research area owns generous solar and thermal resources, with an average annual sunshine duration of 2838.2h and an average annual frost-free period of 214d. The specific time for UAV to collect multispectral images and synchronize ground data is May 14, 2024. Usually, soil leaching solution EC is used to describe the soil salinity status. The higher the soil salinity, the greater the soil EC. 200 soil samples are collected in the research area to ensure the stability and universality of the relationship model between soil measurement and apparent EC. This experiment records information such as sampling depth, longitude, and latitude. After experimental processing, the conductivity of the clear liquid is measured using EICIDDS-307 conductivity meter. The sample EC1:5 is measured. The average EC1:5 value of two soil samples is taken, which is the soil conductivity EC1:5 value at the sampling point. Table 2 shows the parameters for UAV multispectral data collection.

Table 2: Parameter settings for unmanned aerial vehicle multispectral data acquisition

Parameter	DJI Elf 4 multispectral edition plant protection UAV
Flight altitude	200m
Overlap rate of heading shooting	75%
Side shooting overlap	80%
Interval duration	3s
Image resolution	0.30 m
The angle between the multispectral lens and the ground	90

DJI Spirit 4 multi-spectral plant protection UVA is used to collect multi-spectral images. In Table 1-1, the multispectral imaging system integrates five multispectral and one visible light camera containing five wavelength spectral acquisition channels, blue, green, red, NIR, and red edges corresponding to (450±16) nm, (560±16) nm, (650±16) nm, (840±26) nm, and (730±16) nm, respectively. The light intensity sensor integrated at the top

processes the recorded image files to complete the image illumination compensation and eliminate the ambient light noise interference after capturing the solar irradiance. Then the accurate normalized vegetation index NDVI can be obtained. The consistency and accuracy of the data collected in different periods can be maintained. The optical system, image processing technology, the spectral detection algorithm, and other dimensions are integrated by using multi-spectral sensor technology. Then the accurate acquisition of multi-spectral information and the efficient identification of target features can be achieved. The flight altitude of the UAV is set at 200m. The overlap rate of heading shooting is set at 75%. The overlap rate of lateral shooting is set at 80%. The interval between two-point shooting is three seconds. The shooting interval is an equal time interval. The angle between the camera lens and the ground should be 90 degrees. The resolution of the image shot is 0.30m. During performing data acquisition, the pre-planned flight area is imported into DJI GSPro software. The aircraft can complete its flight according to the flight plan. The stored folder is imported into the computer after data collection. Pix4Dmapper software is used to correct and concatenate the single-band images of the study area. In ENVI 5.3 software, various spliced band images are integrated to form a complete image. This study will sort the measured EC values of 200 soil samples collected, with 2/3 of the samples used for modeling and 1/3 for validation and testing.

2.2 Remote sensing image feature extraction

When analyzing whether there is salinization in soil, soil texture characteristics can be effectively utilized. The texture features have significant differences, especially in the surface features, coverage, vegetation types, and other landscape areas of soils with different degrees of salinization. Texture features mainly include four types: statistical, model, signal processing, and structural features. This study combines GLCM and Gabor two-dimensional filters to extract soil texture features. GLCM is a statistical result obtained by maintaining a specific distance between two pixels in an image. $p(i,j,d,\theta)$ forms a matrix that reflects the spatial correlation of grayscale between two points in the image. θ is the direction, which is generally calculated in four directions: 0°, 45°, 90°, and 135° in applications. d represents the interval. If the image has l gray levels, its matrix is represented as $\left[p(i,j,d,\theta)_{l\times l}\right]$. $p(i,j,d,\theta)$ represents the elements in the i-th row and j-th column of the gray level co-occurrence matrix. The final statistical value is expressed in a matrix. The values in the matrix represent different gray levels. Due to the high computational complexity of GLCM, the eight most commonly used features, namely mean, variance, angular second-moment, homogeneity, contrast, correlation, inverse variance, and entropy, are generally used to obtain images' texture features. The mean feature is represented by formula (1).

$$Mean = \sum_i \sum_j \rho(i,j) \tag{1}$$

In formula (1), $\rho(i,j)$ represents the element in row i and column j of GLCM. The higher this value, the more difficult and disorganized the image texture is to describe. The smaller this value, the easier and more regular the texture features are to describe. The variance feature is represented by formula (2).

$$Variance = \sum_i^{N-1} \sum_j^{N-1} \rho(i,j)(i - Mean)^2 \tag{2}$$

The angular second-moment reflects an image's grayscale distribution. The larger this value, the more uniform the grayscale distribution is represented by formula (3).

$$Asm = \sum_i \sum_j \rho(i,j)^2 \tag{3}$$

Contrast represents the brightness contrast between a certain pixel value and pixel values in other fields, reflecting an image's clarity. A larger value refers to a clearer image. Otherwise, this image is blurrier, represented by formula (4).

$$con = \sum_i \sum_j (i,j)^2 \rho(i,j) \tag{4}$$

Homogeneity refers to the local texture changes in an image. If the change is significant, then the matrix value is small. If the change is small, then the matrix value is large, represented by formula (5).

$$H = \sum_{i=0}^{N-1} \sum_{j=0}^{N-1} \frac{i,j|d,\theta}{1+(i-j)^2} \tag{5}$$

In formula (5), d represents the interval between two points in the image. θ represents direction. The entropy feature is represented by formula (6).

$$Ent = \sum_i \sum_j \rho(i,j) \rho \log(i-j) \tag{6}$$

Correlation reflects the similarity in grayscale levels between rows and columns of an image. A larger value refers to greater similarity, represented by formula (7).

$$con = \sum_i \sum_j (ij) \rho(i,j) - \mu_x \mu_y / \sigma_x \sigma_y \tag{7}$$

The inverse variance reflects the local changes in the texture of the image. A larger value refers to more regular image texture, represented by formula (8).

$$Inver = \sum_i \sum_j \rho(i,j) / \left[1+(i-j)^2\right] \quad (8)$$

Gabor filters utilized to extract texture features from high-resolution RS images is a very effective method. A two-dimensional Gabor filter is used in this study. This method consists of a product of a sinusoidal plane wave and a Gaussian kernel, including the real and imaginary parts. The real part is shown in formula (9).

$$g(x,y,\lambda,\theta,\varphi,\gamma) = \exp\left(-\frac{x^2+\gamma^2y^2}{2\sigma^2}\right) \times \exp\left(i\left(2\pi\frac{x}{\lambda}+\varphi\right)\right) \quad (9)$$

In formula (9), λ represents the Gabor filtering wavelength, φ represents the phase shift, σ represents the standard deviation of the Gaussian function, γ represents the spatial aspect ratio, and θ represents the direction of the Gabor kernel function. The representation of the imaginary part is shown in formula (10).

$$g(x,y,\lambda,\theta,\varphi,\gamma) = \exp\left(-\frac{x^2+\gamma^2y^2}{2\sigma^2}\right) \times \cos\left(2\pi\frac{x}{\lambda}+\varphi\right) \quad (10)$$

There are six frequencies. 4 ELM directions include ELM 0, 45, 90, and 135. Then there are a total of 24 kernel functions. This allows for multi-scale and multi-directional extraction of soil texture features. The energy information of Gabor is the most suitable way to express the texture information of images. Using Gabor, an image's texture features are obtained using standard deviation and mean. The Gabor texture feature vector T of the image is defined, represented by formula (11).

$$T(v,\ell) = \left\{M_{0,0}, V_{0,0}, M_{0,1}, V_{0,1}, \ldots, M_{v-1,\ell-1}, V_{v-1,\ell-1}\right\} \quad (11)$$

In formula (11), $M(v,\ell)$ represents the mean of the image. $V(v,\ell)$ represents the standard deviation of the image. The results of T include imaginary part features, real part features, four directions, six frequencies, standard deviation, and mean. Therefore, the final image dimension obtained is 2×4×6×2=96, which is the texture feature of the pixel points in the current region. A 160×160 image sample is selected to improve the classification accuracy. A sliding domain method is adopted. A sliding window with a size of 16×16 is established with a certain pixel point as the center. The sample image is traversed using a Gabor filter. Gabor filters also have a drawback in image processing, namely, the obtained texture feature dimensions are too high. Data are organized using a covariance matrix to achieve dimensionality reduction of high-dimensional feature vectors, represented by formula (12).

$$\operatorname{cov}(X,Y) = \frac{\sum_{i=1}^{n}\left(X_i-\bar{X}\right)\left(Y_i-\bar{Y}\right)}{n-1} \quad (12)$$

Spectral features are a collection of all features that describe the segmented image object and its pixels. Custom spectral feature parameters can improve the classification accuracy in addition to common spectral feature parameters such as mean, brightness, and standard deviation. The Normalized Difference Vegetation Index (NDVI) and salinity index are used to classify saline soil in the study area. According to NDVI, soil salinization information is extracted and expressed using formula (13).

$$NDVI = (NIR-R)/(NIR+R) \quad (13)$$

NIR and R represent the ground reflectance of the near-infrared and red-light bands, respectively. The soil Total Salt Index (TSI) is a parameter that can be used to describe the spatial distribution of soil salinity. The larger the TSI, the greater the difference between soil water, air, and other environmental conditions in the region, resulting in higher salt content and lower water content. TSI is represented by formula (14).

$$TSI = \sqrt{B \times R} \quad (14)$$

In formula (14), B and R represent the reflectance values of red and blue bands in RS images, respectively. The texture segmentation identification method using the Gabor filter is as follows:

(1) First, the input image is read and displayed.

(2) A series of Gabor filters tuned to different frequencies and directions are designed. The tions between [0,150] degrees are sampled at steps of 30 degrees. The sampling wavelength increases with a power of 2, from $4/\sqrt{2}$ to the oblique length of the input image.

(3) The Gabor magnitude features are extracted from the source images. The amplitude response of each filter is usually used when using a Gabor filter. The Gabor amplitude response is sometimes also called the "Gabor energy". The each MxNGabor magnitude output image of the input gabormag (:,:, ind) is the output of the corresponding Gabor filter g (ind).

(4) The post-processing is needed to use the Gabor magnitude response as a classification feature, including Gaussian smoothing. Additional spatial information is added to feature sets. The expected form of pca and kmeans functions is reshaped. The feature information is normalized to common variance and mean.

(5) Simple Gaussian low-pass filtering is then used to smooth the Gabor amplitude information to compensate for the local variation. The sigma that matches the Gabor filter is usually selected to extract each feature. A

smoothing term K is also introduced, which controls the smoothness of the application to the Gabor amplitude response.

(6) The data are reasted into the expected matrix X of the classification function. Each pixel in the image grid is a separate data point. Each plane in the variable feature set is a separate feature.

(7) Finally, the Gabor texture features are classified.

2.3 ELM design for quantitative inversion model of conductivity unmanned aerial vehicle remote sensing

A quantitative inversion model for EC UAV RS based on ELM is constructed after extracting the texture and spectral features of RS images in the research area. ELM can be regarded as a feedforward neural network, which typically presents better classification performance with relatively fewer constraints and has relatively better generalization ability. Using ELM for training, the weights and bias values of the hidden layer nodes can be generated randomly using any continuous probability distribution, rather than being generated through other methods. ELM is more efficient than traditional Support Vector Machine (SVM) and Back Propagation Neural Network (BPNN). ELM randomly constructs the input and hidden layers' connection weights. The hidden layer neurons' threshold is constructed, which is not adjusted during training. ELM only needs to set the hidden layer neurons. Meanwhile, ELM performs a simple generalized inverse operation on the hidden layer's output matrix H. The connection weights formed by the hidden and output layers can be computed, achieving the effect of approximating a continuous system. Figure 1 presents ELM's network structure.

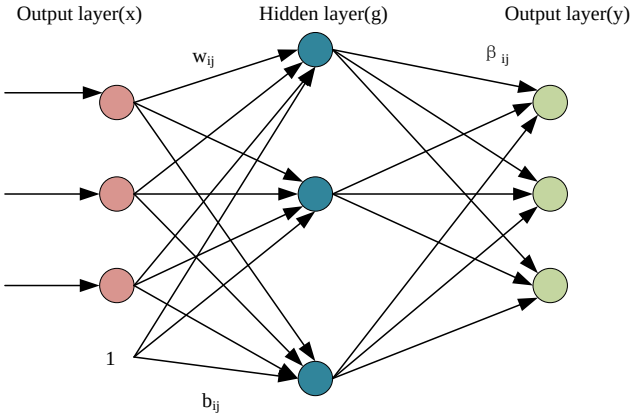

Figure 1: ELM network structure

In Figure 1, when the total hidden neurons are L, which contain N different samples (x_i, y_i). The input is $x_i = [x_{i1}, x_{i2}, ..., x_{in}]_T \in R^n$ and the output is $y_i = [y_{i1}, y_{i2}, ..., y_{im}]_T \in R^m$. Assuming the hidden layer's activation function is $g(x)$, this function can be any nonlinear piecewise continuous function. At this point, the output of ELM is represented by formula (13).

$$y_j = f(x) = \sum_{i=1}^{L} \beta_i g(x_j w_i + b_i), j = 1, 2, ..., N \quad (13)$$

In formula (13), $w_i = [w_{i1}, w_{i2}, ..., w_{in}]^T$ represents a weight between the i th neuron connecting the input and hidden layers. $\beta_i = [\beta_{i1}, \beta_{i2}, ..., \beta_{im}]^T$ refers to the i th neuron and the output layer's weight. b_i refers to the i th hidden layer neuron's critical value. The simplified expression of the network model output by ELM is represented by formula (14).

$$\begin{cases} Y = H\beta \\ H = \begin{bmatrix} g(w_1 x_1 + b_1) & \cdots & g(w_L x_1 + b_L) \\ \vdots & \ddots & \vdots \\ g(w_1 x_N + b_1) & \cdots & g(w_L x_N + b_L) \end{bmatrix} \end{cases} \quad (14)$$

In formula (14), H refers to the hidden layer node's output local matrix. β refers to a weight matrix hidden in the output layer. Y refers to an output matrix. When an activation function $g(x)$ is infinitely differentiable, the obtained objective function is represented by formula (15).

$$\min_{\beta} \|H\beta - Y\| \quad (15)$$

In formula (15), $\beta \in R^{L\times m}$. The optimal solution of the objective function is represented by formula (16).

$$\hat{\beta} = H^{+}Y \tag{16}$$

In formula (16), H^{+} refers to the Moore-Penrose generalized inverse of the hidden output matrix H. The problem at this point becomes finding the computational matrix H 's Moore-Penrose generalized inverse matrix. This can be solved using methods such as orthogonalization, iteration, and singular value decomposition. After constructing the research model, specific evaluations of the model accuracy are conducted using determination coefficient (R^2), Root Mean Square Error (RMSE), and Relative Percentage Deviation (RPD).

3 Results

3.1 Model performance evaluation

Machine learning algorithms were used to validate the most commonly used standard test dataset UCI database. This proposed classification model's accuracy and effectiveness were verified. The UCI standard dataset was used for experimental validation to more accurately compare research algorithms. Genetic algorithm optimized extreme learning machine parameter model (GA-ELM) and artificial bee colony algorithm optimized extreme learning machine parameter model (ABC-ELM) were selected as comparative methods. In the validation experiment, first, the properties of the data set were normalized. 20% of the required validation data set was the test set. 80% of the set was the training set for the parameter optimization of the research algorithm. Each model was validated in UCI data set for 10 iterations. In the parameter setting of GA-ELM, its population selection was 20, with a crossover probability of 0.85, variation probability of 0.0085, and crossover probability of 0.8. In the parameter selection of ABC-ELM, the population selection agreed with the previous two algorithms was 20. The number of solutions was 2. In the parameter optimization of the three models, the condition for their final stop iteration was the same, that is, all models reached the maximum iteration. The effect of the proposed algorithm model, RF, GA-ELM, and ABC-ELM algorithms on classifying the Blood and Glass datasets in the UCI database is shown in Figure 2.

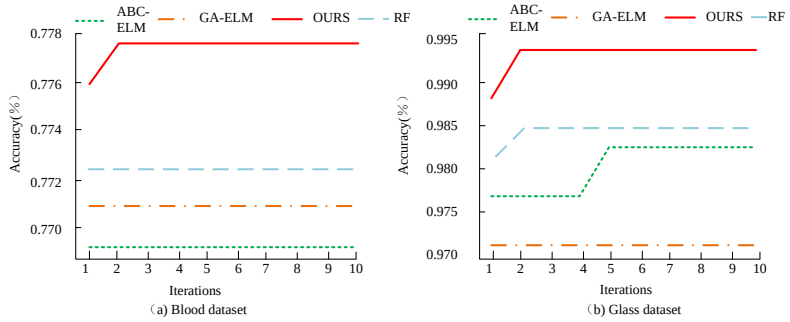

Figure 2: Classification performance of different algorithms on the UCI dataset

From Figure 2, the proposed algorithm in the Blood and Glass UCI datasets showed good classification effects regardless of the application of data properties in high or low dimensions and the categories in the data set. The experimental results were evaluated and analyzed for both classification accuracy and running time. The selecting results the specific parameters and the corresponding optimal accuracy of the four algorithms were also calculated. The experimental results are shown in Figure 3.

Figure 3: Comparison of three optimal classification results for datasets

From Figure 3, the accuracy of the study algorithm in Blood and Glass dataset was 77.76% and 99.41%, respectively, which was better than GA-ELM, RF, and ABC-ELM algorithms. The classification accuracy of the study algorithm was higher than GA-ELM by 0.66%-4%, ABC-ELM by 0.4%-5.33%, and RF by 3.51%-14.4%. The results showed that the proposed algorithm model was effective and could be used to detect and evaluate soil conductivity.

3.2 Correlation analysis between remote sensing image features and soil conductivity

The study obtained 24 texture features from three spectral channels, including red, green, and blue. Each channel extracted 8 image features including mean, variance, homogeneity, et al. Texture features were obtained by utilizing GLCM from the ENVI5.3 toolbox. The texture analysis used a 3×3 window and a 90-degree direction to calculate feature values. Table 3 shows the results.

Table 3: Correlation analysis between texture features and soil conductivity

Texture features	Red light channel	Green light channel	Blue light channel
Mean	0.31	0.27	0.34
Variance	0.35	0.32	0.31
Homogeneity	0.34	0.24	0.29
Contrast	0.21	0.19	0.23
Dissimilarity	0.22	0.21	0.17
Entropy	0.33	0.26	0.29
Second-moment	0.21	0.22	0.2
Correlation	0.26	0.22	0.21

From Table 3, overall, the correlation between the texture features extracted from the three channels and soil EC was ranked in descending order: red light channel>blue light channel>green light channel. The correlation coefficient between texture features and soil EC ranged from 0.17 to 0.35. The texture features' correlation coefficient extracted from the red-light channel and soil EC was between 0.21 and 0.35. The correlation between contrast and second-moment with soil EC was the worst, with a correlation coefficient of only 0.21. The correlation coefficient between the texture features extracted from the green light channel and soil EC was between 0.21 and 0.32. The correlation coefficient between the texture features extracted from the blue light channel and soil EC was between 0.17 and 0.34. The correlation between heterogeneity and soil EC was the worst, with a correlation coefficient of only 0.17. Figure 4 shows soil EC and spectral index's correlation.

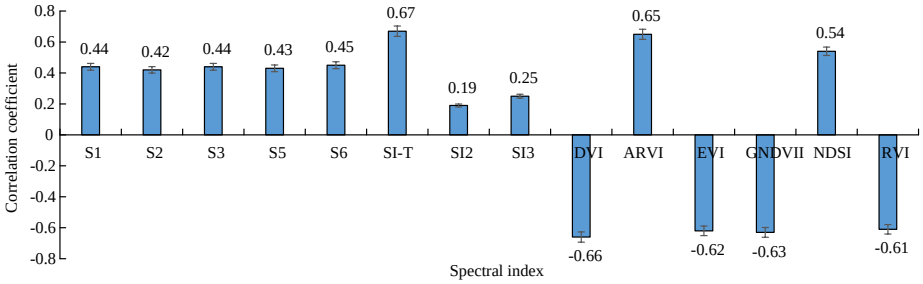

Figure 4: Correlation between soil conductivity and spectral index

From Figure 4, overall, there was a good correlation between the selected spectral index and soil EC, with absolute correlation coefficients located in 0.19~0.67. The salinity indices ARVI, SI-T, NDSI, S6, S1, S3, S5, S2, SI3, and SI2 had positive connection with soil EC. The vegetation indices DVI, GNDVI, EVI, and RVI had negative connection with soil EC. The correlation coefficients of SI-T, DVI, ARVI, GNDVI, EVI, and RVI all exceeded 0.6. The correlation between SI-T and soil EC was the highest, at 0.67. The correlation between SI2 and soil EC was the weakest, at 0.19. This indicated that the spectral indices selected in this study could characterize soil EC to some extent.

3.3 Soil conductivity monitoring and evaluation

The 24 texture features extracted from three channels were used as model inputs. Based on research algorithms, a soil EC estimation model based on texture features was constructed and compared with SVM and BPNN. Figure 5 shows the performance evaluation results of different models.

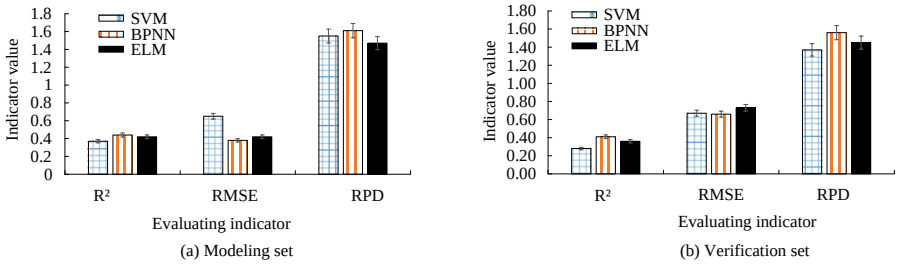

Figure 5: Validation results of soil conductivity estimation model based on texture features

From Figure 5, the accuracy of the three soil EC estimation models constructed using texture features as model inputs ranged from 0.37 to 0.42, all of which reached above 0.30. This soil EC estimation model based on BPNN is the best, having R^2 of 0.44, RMSE of 0.38dSm-1, and RPD of 1.61, indicating that BPNN had a good effect on estimating soil EC. Next was the ELM soil EC estimation model, with R^2 of 0.42, RMSE of 0.42 dSm-1, and RPD of 1.47. The SVM soil EC estimation model had the worst performance, with R^2 of 0.37, RMSE of 0.65dSm-1, and RPD of 1.55. Overall, the estimation accuracy of using texture features alone to construct soil EC models was not ideal, with R^2 below 0.5, which could not accurately estimate soil EC selection. 50 samples from the validation set were used to validate three models. Figure 6 presents the fit between the predicted and measured values.

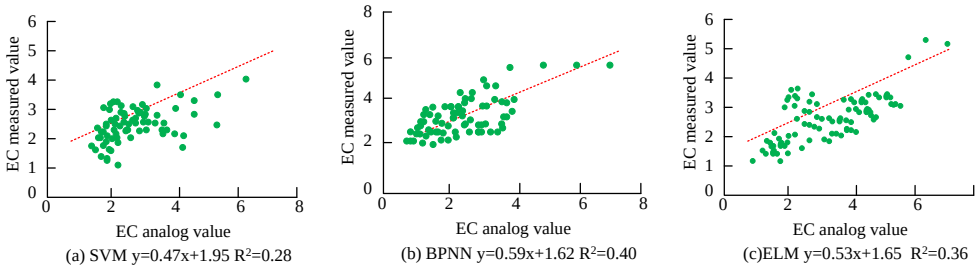

Figure 6: Actual and predicted values of soil conductivity in the validation set

From Figure 6, the R^2 for SVM, BPNN, and ELM estimation models was 0.28, 0.41, and 0.36, respectively. The RMSE was 0.67dSm-1, 0.66dSm-1, and 0.73dSm-1, respectively. The RPD was 1.37, 1.56, and 1.45, respectively. The R^2 of the validation set model was above 0.25. The evaluation indicators of the validation set and the modeling set were relatively close, without overfitting phenomenon. Therefore, the accuracy of SVM and ELM estimation models was lower than that of BPNN, which had higher RMSE than BPNN. The RPD of BPNN was greater than 1.6, and its predictive and stability performance were better.

The selected spectral index could be used as a model input for estimating soil EC research. The 14 extracted spectral indices were used as the model's inputs. Based on the research algorithm, a soil EC estimation model based on texture features was constructed and compared with SVM and BPNN. Figure 7 shows the model accuracy verification results.

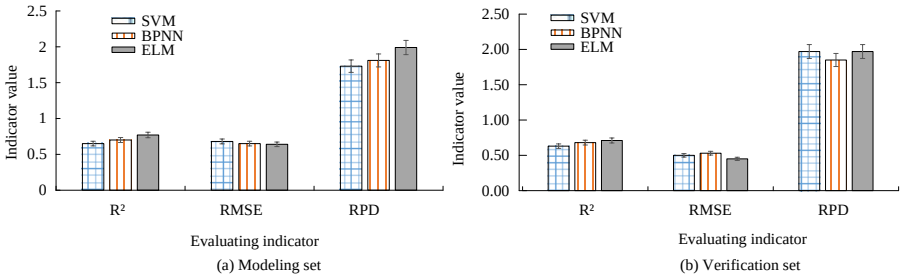

Figure 7: Validation results of soil conductivity estimation model based on spectral index

From Figure 7, the accuracy of these three soil EC estimation models constructed with spectral index as the model input was between 0.65 and 0.77, all reaching above 0.60. This soil EC estimation method on the foundation of ELM was the best estimation model, with the best model evaluation results, R^2 of 0.77, RMSE of 0.64dSm-1, RPD of 1.99, indicating a relatively ideal estimation effect. When using spectral index as the model input, ELM had better prediction accuracy for soil EC and could better express soil EC information. Next was the BPNN soil EC estimation model, with R^2 of 0.70, RMSE of 0.65dSm-1, and RPD of 1.81. Compared to texture features as input for the model, this model's accuracy was greatly enhanced. This SVM soil EC estimation method is the worst, with R^2 of 0.65, RMSE of 0.68 dSm-1, and RPD of 1.73. Using spectral index as the model input to construct a soil EC estimation model, its estimation accuracy was higher and more stable compared to texture feature models. Three models were validated using a validation set. Figure 8 shows the fit between the predicted and measured values obtained.

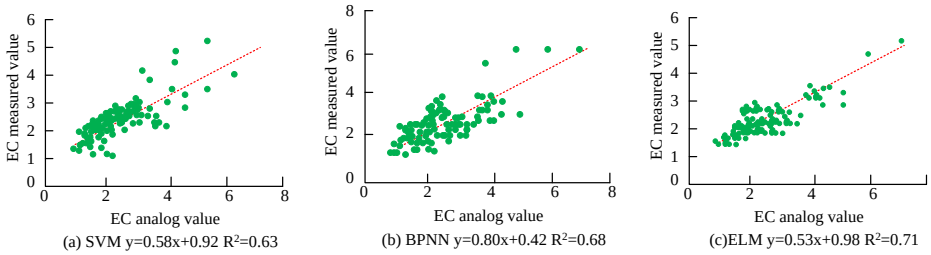

Figure 8: Actual and predicted values of soil conductivity in the validation set

From Figure 8, the R^2 of SVM, BPNN, and ELM estimation models was 0.63, 0.68, and 0.71, respectively. The model accuracy in the validation set was above 0.60. The difference in evaluation indicators between the validation set and the modeling set was not significant, indicating that the model performance was relatively stable. The effect of ELM was the most significant, followed by BPNN. The modeling effect of SVM was not ideal. Compared with traditional analysis methods, machine learning methods greatly enhanced this model's accuracy and stability, which had strong ability to handle nonlinear mappings.

All 14 spectral indices and 24 texture features extracted from UAV multispectral images were used as input variables to further improve the model's estimation accuracy. Therefore, a soil EC estimation model based on feature fusion was constructed. Figure 9 shows the results of the estimation models.

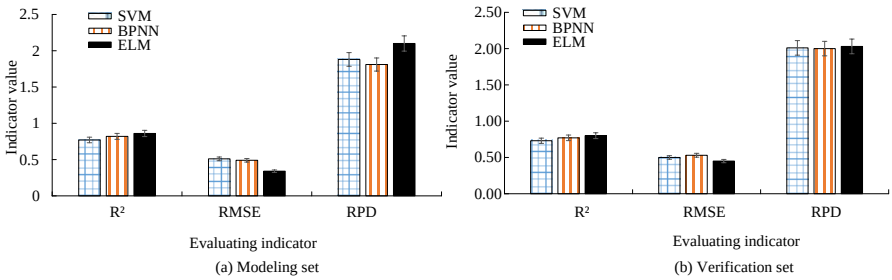

Figure 9: Validation results of soil conductivity estimation model based on feature fusion

From Figure 9 (a), the R^2 of all three estimation models was greater than 0.75, with RPD greater than 1.80. The estimation model based on ELM had the best performance, with the highest R^2, RPD, and lowest RMSE (R^2=0.86, RMSE=0.34dSm-1, RPD=2.10). This indicated that the combination of feature fusion method and ELM had strong estimation ability for soil EC. Next was BPNN, with R^2 of 0.82, RMSE of 0.49 dSm-1, and RPD of 1.81. The SVM estimation model had the lowest performance, with an R^2 of 0.77, an RMSE of 0.51dSm-1, and an RPD of 1.88. However, the accuracy of the SVM estimation model also improved with different model inputs. From Figure 9 (b), the R^2, RMSE, and RPD based on ELM were 0.80, 0.45 dSm-1, and 2.03, respectively, which were also the optimal model among these three models. Next was BPNN, with R^2, RMSE, and RPD of 0.77, 0.53dSm-1, and 2.00, respectively. The SVM estimation model's accuracy was higher than that of ELM and BPNN, with R^2, RMSE, and RPD of 0.73, 0.50 dSm-1, and 2.01, respectively. The difference in evaluation indicators between the modeling and validation set models was relatively small. This indicated that the model estimation was improved after unifying spectral index and texture features as input variables. The overfitting phenomenon that existed was eliminated.

4 Discussion

Soil salinization is a major agricultural problem and can reduce crop yields. The monitoring of soil salinization often requires expensive costs and manual laboratory measurements. However, the UAV RS technology is not restricted by the above factors and can monitor the research area at high frequency and for a long time. The research aims at exploring the potential of the UAV RS technology to estimate soil salinity in cotton fields during the reproductive period. Some scholars have demonstrated the ability of soil salinization based on UAV images. This study uses a machine learning model to monitor soil conductivity in cotton fields. The quantitative inversion model is conducted by fusing spectral and texture feature information based on ELM soil conductivity. The results showed that this model had the modeling set coefficient of determination of 0.77, 0.82, and 0.86, respectively. Its prediction sets coefficient was 0.73, 0.77, and 0.80, respectively. The quantitative inversion model had the highest prediction accuracy. Compared with SVM, ELM often produced better performance with less optimization constraints and good generalization ability. It is more efficient than traditional BPNN, which is the same as the method proposed by Wang et al. [20]. The soil salinity inversion model was established for different salinization grades. The final test results showed that ELM was the optimal monitoring model. In conclusion, compared with other machine learning algorithms, ELM is promising for quantitative soil salinity research. The study used texture information, vegetation index, and the collection of two data sets. Then the influence of different feature input quantity on the predictive ability of soil conductivity monitoring model was compared. In the study, the model constructed using feature fusion had higher prediction accuracy, followed by the vegetation index. The texture index model was relatively poor effect. Traditional soil salt measurement is usually estimated by the salt index method in the bare soil period. Some scholars have also discussed the research of UAV multispectral RS technology in soil salt content under different vegetation coverage. Hu constructed the soil salt based on three input variable group RS inversion model. The multiple regression, partial least squares regression, limit learning machine, SVM, and BPNN were used. The multiple regression model had the best inversion effect in the six linear regression model. BPNN built on the whole variable group inversion model had the highest accuracy [21]. However, the inversion model accuracy is still not as good as the research model. This is because UAV multispectral RS can directly obtain the relevant data of the soil surface to reverse the soil salinity. In vegetation coverage, the use of UAV RS of soil salt estimation is mainly reflected in the vegetation state of growth. Crops mainly absorb soil moisture organs mainly root. The impact of soil salinity changes on crop water absorption is relatively significant, thus hindering crop growth. The soil salinity is relatively high. Crops have unhealthy growth. This is mainly from the crown parts of the crops. The vegetation index is based on the reflection spectral characteristics of vegetation. Various combinations of wave bands are used to obtain the growth and development of crops.

5 Conclusion

The traditional soil salinization monitoring method has problems such as high cost, low speed, and low efficiency in obtaining soil salinization information. ELM was used to monitor soil EC in cotton fields. An EC UAV RS quantitative inversion model based on ELM was proposed. The modeling set's R^2 of SVM, BPNN, and ELM soil EC quantitative inversion models constructed with texture features as input was 0.37, 0.44, and 0.42, respectively. The prediction set's R^2 was 0.28, 0.41, and 0.36, respectively. BPNN had higher prediction accuracy. The salinity indices ARVI, SI-T, NDSI, S6, S1, S3, S5, S2, SI3, and SI2 were positively correlated with soil EC, with correlation coefficients located in 0.19~0.67. The correlation between SI-T and ARVI was significantly higher than the other 8 spectral indices, having correlation coefficients of 0.67 and 0.65, respectively. The vegetation indices DVI, GNDVI, EVI, and RVI were negatively correlated with soil EC, with correlation coefficients located in -0.66~-0.60. The SVM, BPNN, and ELM soil EC quantitative inversion models constructed using vegetation indices all had high accuracy. The modeling set's R^2 was 0.65, 0.70, and 0.77, respectively. The prediction set's R^2 was 0.63, 0.68, and 0.71, respectively. ELM's accuracy was higher than that of SVM and BPNN. A quantitative inversion model for soil EC was constructed

using 14 spectral indices and 24 texture feature information. The modeling set's R^2 was 0.77, I0.82, and 0.86, respectively. The prediction set's R^2 was 0.73, 0.77, and 0.80, respectively. ELM had the highest prediction accuracy. Finally, this soil EC estimation model using ELM was the optimal model, achieving precise monitoring of soil EC. However, the universality of this model is poor. Multiple different experimental areas have not been studied. Further exploration will be conducted in other semi-arid and arid areas.

Fundings

The research is supported by: 2022 Jiangxi Provincial Department of Education Science and Technology Research Project "Research on Forest Fire Monitoring System Based on Multi rotor Unmanned Aerial Vehicle" (No. GJJ2210202).

References

[1] K. Ismoilova, T. Kuliyev, N. Sultonova, and S. Karimova, "Correlations between quantitative indicators of photosynthetic pigments in vicia varieties under conditions of soil salinization," Journal of Stress Physiology & Biochemistry, vol. 20, no. 1, pp. 117-124, 2024.

[2] L. Wang, and L. Zhang, "A review on the improvement of saline-alkali soil by organic fertilizer," Academic Journal of Science and Technology, vol. 10, no. 3, pp. 10-11, 2024. https://doi.org/10.54097/80pha530

[3] H. Yu, Z. Wang, D. Mao, M. Jia, S. Chang, and X. Li, "Spatiotemporal variations of soil salinization in China's West Songnen Plain," Land Degradation and Development, vol. 34, no. 8, pp. 2366-2378, 2023. https://doi.org/10.1002/ldr.4613

[4] B. Guo, M. Lu, Y. Fan, H. Wu, Y. Yang, and C. Wang, "A novel remote sensing monitoring index of salinization based on three-dimensional feature space model and its application in the Yellow River Delta of China," Geomatics, Natural Hazards and Risk, vol. 14, no. 1, pp. 95-116, 2022. https://doi.org/10.1080/19475705.2022.2156820

[5] Y. Inoue, "Satellite-and drone-based remote sensing of crops and soils for smart farming-a review," Soil Science and Plant Nutrition, vol. 66, no. 6, pp. 798-810, 2020. https://doi.org/10.1080/00380768.2020.1738899

[6] R. N. Sahoo, R. G. Rejith, S. Gakhar, R. Ranjan, M. C. Meena, A. Dey, J. Muknerjee, R. Dhajar, A. Meena, A. Daas, S. Babu, R. K. Upadhyay, K. Sekhawat, S. Kumar, M. Kumar, V. Chinnusamy, and M. Khanna, "Drone remote sensing of wheat N using hyperspectral sensor and machine learning," Precision Agriculture, vol. 25, no. 2, pp. 704-728, 2024. https://doi.org/10.1007/s11119-023-10089-7

[7] D. Olson, and J. Anderson, "Review on unmanned aerial vehicles, remote sensors, imagery processing, and their applications in agriculture," Agronomy Journal, vol. 113, no. 2, pp. 971-992, 2021. https://doi.org/10.1002/agj2.20595

[8] F. H. Iost Filho, W. B. Heldens, Z. Kong, and E. S. de Lange, "Drones: Innovative technology for use in precision pest management," Journal of economic entomology, vol. 113, no. 1, pp. 1-25, 2020. https://doi.org/10.1093/jee/toz268

[9] P. K. R. Maddikunta, S. Hakak, M. Alazab, S. Bhattacharya, T. R. Gadekallu, W. Z. Khan, and Q. Pham, "Unmanned aerial vehicles in smart agriculture: Applications, requirements, and challenges," IEEE Sensors Journal, vol. 21, no. 16, pp. 17608-17619, 2021. https://doi.org/10.1109/JSEN.2021.3049471

[10] K. M. Gojiya, H. D. Rank, P. M. Chauhan, D. V. Patel, P. M. Satasiya, and P. Gisish, "Remote sensing and GIS applications in soil salinity analysis: A comprehensive review," International Journal of Environment and Climate Change, vol. 13, no. 11, pp. 2149-2161, 2023. https://doi.org/10.9734/IJECC/2023/v13i113377

[11] R. Mahadasa, P. Surarapu, V. R. Vadiyala, and P. R. Baddam, "Utilization of agricultural drones in farming by harnessing the power of aerial intelligence," Malaysian Journal of Medical and Biological Research, vol. 7, no. 2, pp. 135-144, 2020.

[12] X. Cui, W. Han, H. Zhang, J. Cui, W. Ma, L. Zhang, and G. Li, "Estimating soil salinity under sunflower cover in the hetao irrigation district based on unmanned aerial vehicle remote sensing," Land Degradation & Development, vol. 34, no. 1, pp. 84-97, 2023. https://doi.org/10.1002/ldr.4445

[13] B. Guo, M. Lu, Y. Fan, H. Wu, Y. Yang, and C. Wang, "A novel remote sensing monitoring index of salinization based on three-dimensional feature space model and its application in the Yellow River Delta of China," Geomatics, Natural Hazards and Risk, vol. 14, no. 1, pp. 95-116, 2023. https://doi.org/10.1080/19475705.2022.2156820

[14] S. Pal, A. Roy, P. Shivakumara, and U. Pal, "Adapting a swin transformer for license plate number and text detection in drone images," Artificial Intelligence and Applications, vol. 1, no. 3, pp. 145-154, 2023. https://doi.org/10.47852/bonviewAIA3202549

[15] S. Meivel, and S. Maheswari, "Remote sensing analysis of agricultural drone," Journal of the Indian Society of Remote Sensing, vol. 49, no. 3, pp. 689-701, 2021. https://doi.org/10.1007/s12524-020-01244-y

[16] H. Webb, N. Barnes, S. Powell, and C. Jones, "Does drone remote sensing accurately estimate soil pH in a spring wheat field in southwest montana?." Precision Agriculture, vol. 22, no. 6, pp. 1803-1815, 2021. https://doi.org/10.1007/s11119-021-09812-z

[17] R. N. Sahoo, R. G. Rejith, S. Gakhar, R. Ranjan, M. C. Meena, A. Dey, J. Muknerjee, R. Dhajar, A. Meena, A. Daas, S. Babu, R. K. Upadhyay, K. Sekhawat, S. Kumar, M. Kumar, V. Chinnusamy,

and M. Khanna, “Drone remote sensing of wheat N using hyperspectral sensor and machine learning,” Precision Agriculture, vol. 25, no. 2, pp. 704-728, 2024. https://doi.org/10.1007/s11119-023-10089-7

[18] V. N. Lednev, M. Y. Grishin, P. A. Sdvizhenskii, V. A. Zavozin, A. F. Bunkin, P. K. Kurbanov, M. A. Litvinov, O. N. Tretinnikov, and S. Pershin, “Drone based fluorescence LIDAR for agriculture fields in situ diagnostics,” Bulletin of the Lebedev Physics Institute, vol. 50, no. 3, pp. 103-107, 2023. https://doi.org/10.3103/S1068335623030065

[19] X. Jiang, H. Duan, J. Liao, P. Guo, C. H. Huang, and X. Xue, “Comparative research on multi-algorithm of soil salinity monitoring based on Gaofen-5, Sentinel-1, and Sentinel-2,” International Journal of Remote Sensing, vol. 44, no. 15, pp. 4704-4726, 2023. https://doi.org/10.1080/01431161.2023.2235640

[20] D. Wang, H. Chen, Z. Wang, and Y. Ma, “Inversion of soil salinity according to different salinization grades using multi-source remote sensing,” Geocarto International, vol. 37, no. 5, pp. 1274-1293, 2022. https://doi.org/10.1080/10106049.2020.1778104

[21] X. Hu, B. Niu, X. Li, and X. Min, “Unmanned aerial vehicle (UAV) remote sensing estimation of wheat chlorophyll in subsidence area of coal mine with high phreatic level,” Earth Science Informatics, vol. 14, no. 4, pp. 2171-2181, 2021. https://doi.org/10.1007/s12145-021-00676-5